Research article

Gaofeng Liang, Xi Chen, Qing Zhao* and L. Jay Guo*

Achieving pattern uniformity in plasmonic lithography by spatial frequency selection

https://doi.org/10.1515/nanoph-2017-0028
Received February 22, 2017; revised May 29, 2017; accepted June 11, 2017

Abstract: The effects of the surface roughness of thin films and defects on photomasks are investigated in two representative plasmonic lithography systems: thin silver film-based superlens and multilayer-based hyperbolic metamaterial (HMM). Superlens can replicate arbitrary patterns because of its broad evanescent wave passband, which also makes it inherently vulnerable to the roughness of the thin film and imperfections of the mask. On the other hand, the HMM system has spatial frequency filtering characteristics and its pattern formation is based on interference, producing uniform and stable periodic patterns. In this work, we show that the HMM system is more immune to such imperfections due to its function of spatial frequency selection. The analyses are further verified by an interference lithography system incorporating the photoresist layer as an optical waveguide to improve the aspect ratio of the pattern. It is concluded that a system capable of spatial frequency selection is a powerful method to produce deep-subwavelength periodic patterns with high degree of uniformity and fidelity.

Keywords: surface plasmon; plasmonic lithography; roughness.

***Corresponding authors: L. Jay Guo,** Department of Electrical Engineering and Computer Science and Applied Physics, University of Michigan, Ann Arbor, MI 48109, USA, e-mail: guo@umich.edu; and **Qing Zhao,** School of Physical Electronics, University of Electronic Science and Technology of China, Chengdu 610054, China, e-mail: zhaoq@uestc.edu.cn
Gaofeng Liang: Department of Electrical Engineering and Computer Science, University of Michigan, Ann Arbor, MI 48109, USA; and School of Physical Electronics, University of Electronic Science and Technology of China, Chengdu 610054, China
Xi Chen: Department of Electrical Engineering and Computer Science and Applied Physics, University of Michigan, Ann Arbor, MI 48109, USA

1 Introduction

Plasmonic-based photolithography has the ability to achieve features beyond the typical diffraction limit. This capability was accomplished by exploiting the surface plasmon (SP) waves confined to the interface between dielectric and metal materials, whose wavelength can be far smaller than that of the light in air [1–3]. For example, "superlens" imaging-based patterning approaches have achieved subwavelength resolution by using a thin slab of metal to amplify the transverse magnetic (TM) polarized evanescent waves [4, 5], therefore capturing the detailed evanescent components to reconstruct a faithful replica of the patterns on the mask with high resolution. In contrast, such evanescent information is mostly lost in traditional projection-based photolithography due to the limited numerical aperture of the exposure system [6]. On the other hand, patterns with high degree of uniformity and certain aspect ratio are required for most of the real-world applications. Unlike traditional projection lithography that uses either 4:1 or 5:1 reduction of the mask pattern [7], the superlens approach yields essentially a 1:1 imaging with very shallow resist depth. This makes the fabrication of photomasks very challenging, especially down to the ~10 nm scale where the edge and surface roughness of the mask or thin film are inevitable. It is well known that a nanoscale asperity of metals such as silver (Ag) generates localized SP resonance with intensified near-field light. The roughness effect on the properties of metal films and particles [8–11], especially Ag superlens [12–14], has been investigated in some recent works. For example, it has been shown that quasi-periodic "roughness" can enhance the resolution of the superlens-based approach [12]. However, one serious question to consider is whether any random roughness on mask patterns or films fundamentally limits the plasmonic-based lithography by amplifying any defects into the exposed photoresist (PR). In other works, a stacked metal/dielectric multilayer structure was proposed to obtain super-resolution by various means including spherical hyperlens [15, 16] and negative refraction [17]. Especially, a hyperbolic metamaterial (HMM)-based structure can be designed as a filter to

allow waves with high spatial frequency to pass through, and suppress other spatial frequencies [18]. Because thin metallic and dielectric films are required to achieve efficient coupling between the SPs at each metal and dielectric interface, similar questions regarding the impacts of the roughness of the mask or the thin film on the pattern quality are raised. Indeed, it has been shown in several studies that film roughness distorts the normal propagation and coupling of waves especially in nanoscale films [14, 19–23], leading to non-uniform PR patterns with poor profiles [24]. All these concerns put critical restrictions on the plasmonic-based lithography for practical applications. Thus, it is important to investigate the effects of the surface roughness and line-edge roughness (LER) on the performance of plasmonic lithography, which is helpful for the design and estimation of plasmonic systems.

In this work, two representative lithography systems are considered, where the effects of roughness in superlens and HMM-based approaches are analyzed systematically. In both cases, deep subwavelength periodic patterns are used, not only because dense line and spacing patterns have traditionally been used as a gold standard for evaluating lithography performance, but also because they have numerous applications in microelectronics, photonics and in other related fields [25–29]. The broad optical transfer function (OTF) of smooth superlens enables a wide range of high wavevector evanescent waves to pass through; meanwhile, the broad OTF also causes the superlens to suffer severely from the roughness of the thin film and isolated defects on the mask. In contrast, the OTF of the HMM presents a spatial frequency selection characteristic, producing uniform and stable interference patterns in the PR layer. It is found that the profile and intensity of the patterns produced by the HMM system are much more immune to the imperfections of the thin film and the mask than those of the patterns produced by the superlens system. This observation is further supported by analyzing a recently reported approach where the PR was incorporated in an optical waveguide to significantly improve the pattern depth [30]. These analyses show that a system capable of spatial frequency selection is a robust approach to produce uniform deep-subwavelength periodic patterns that are insensitive to the imperfections of the films and photomasks.

2 Effect of rough films in photolithography

To fully capture the effects of surface roughness on the performance of the two different lithography systems, a series of three-dimensional structures were simulated using a commercial solver based on the finite element method (COMSOL Multiphysics, COMSOL Inc., Stockholm, Sweden). The roughness of the films in both systems is numerically modeled with random roughness and defects, where the surface roughness is defined as the root-mean square (RMS), i.e. standard deviation of the topography. The properties of the rough surfaces in the simulations are similar to those obtained from measurement (more details are shown in Supplementary S1).

Usually, the superlens system uses a single Ag film to achieve sub-diffraction limited imaging [4, 5, 31]. In this work, a Ag film with the thickness of 20 nm is analyzed with different degrees of roughness. A chromium (Cr) mask with the thickness of 50 nm and the period of 90 nm on a glass substrate is placed above the superlens with a dielectric spacer, which is assumed to be polymethylmethacrylate (PMMA), but the exact nature of the spacer is not critical. A PR film with the thickness of 40 nm is used to record the latent image of the mask. To enhance the contrast of the field intensity, a reflector composed of a Ag film with the thickness of 50 nm is added to the bottom of the PR film [32]. A TM polarized light with the wavelength of 365 nm is incident from the top side, as shown in Figure 1A. The corresponding permittivities of Cr and Ag at the 365 nm wavelength are $\varepsilon_{Cr} = -8.55 + 8.96i$ [33] and $\varepsilon_{Ag} = -2.4 + 0.25i$ [34], respectively. Meanwhile, the permittivities of PMMA, substrate and PR are 2.25, 2.13 and 2.56, respectively. On the other configuration, an HMM composed of an alternating metal/dielectric multilayer is designed (Figure 1B), with the OTF featuring a distinctive filter behavior. The transmitted diffraction orders interfere and produce uniform periodic patterns in the PR film. As an example, we use the work reported in reference [18] and design the corresponding stacked HMM to pass the ±second-order diffracted waves of the grating. To produce a similar pattern size as in the superlens case, a grating type Cr mask is used with the period of 360 nm (i.e. four times that of the mask period in the Ag superlens case). The mask has a much larger period than the reduced patterns, so the mask can be fabricated by conventional UV lithography or laser interference lithography [26–28]. The HMM is composed of nine layers of aluminum (Al) (15 nm) and silicon dioxide (SiO_2) (30 nm) films, which makes the spatial frequency of the desired diffraction orders coincide with the peak of transmission in the OTF. The parameters including the metal filling factor, the thickness of a periodic unit, and the number of films which affect the HMM's lithography performance are discussed in Supplementary S2. The reflective film is an Al film with the thickness of 50 nm. The permittivity of Al at 365 nm wavelength

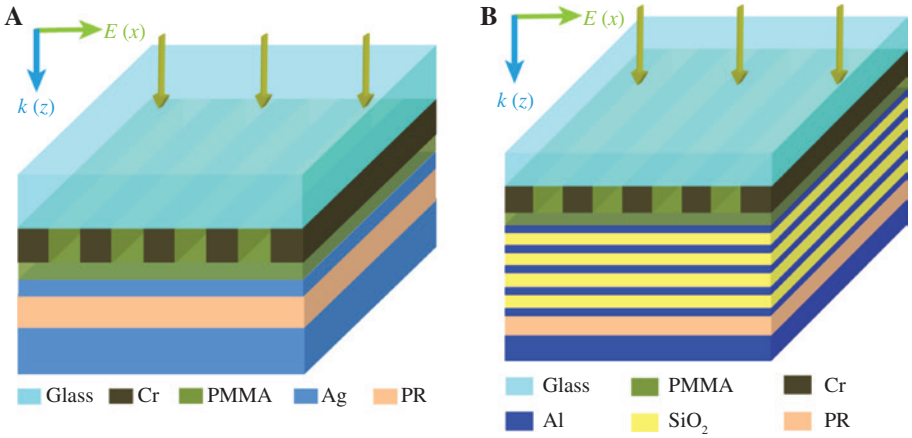

Figure 1: Schematics of plasmonic lithography based on the (A) superlens structure and (B) HMM structure.

is $\varepsilon_{Al} = -19.4 + 3.6i$ [33]. Others parameters are the same as those of the superlens lithography system.

For an ideal superlens system, all the evanescent components of the object should be transmitted through a perfect lens and captured by the PR in order to reconstruct a faithful image [4, 6]. Any loss or distortion of the high-k components inevitably affects the quality of the pattern in the PR film [19, 20, 35]. We use the OTF in k-space to analyze and gain the understanding of the two systems. First, the OTF of the Ag film superlens is calculated by the transfer matrix method (TMM) [36, 37] and simulated by the COMSOL Multiphysics solver, as shown in Figure 2A. For the smooth Ag films, the dashed and solid black curves agree very well, and both show a broad transmission passband. Such a broad OTF enables the evanescent waves of wide wavevector range to pass through the superlens. Therefore, a high-fidelity pattern can be produced in the PR film. Here, we calculate only the OTF of a single Ag film in dielectric media. The OTF of the whole imaging system including the thin PR and reflective films is shown in Supplementary S3. In that case, the OTF still presents a broad passband though the amplitude of the high-k region drops quickly. A two-dimensional (2D) electric field intensity distribution imaged from the 90-nm-period grating mask is shown in Figure 2B. The cross-section taken from the middle position of the PR film shows a uniform pattern with straight profiles and high-intensity contrast (Figure 2C). However, when the roughness is introduced into the two surfaces of the Ag film, the field distribution is severely distorted. Figure 2E shows the intensity distribution of the light passing through the Ag film with the surface roughness of RMS = 2 nm, where the intensity at the rough spots is significantly enhanced locally. Meanwhile, the intensity of the patterns in the PR film is reduced dramatically (Figure 2D), which is in agreement with the reduced transmission amplitude in the OTF (blue curve in Figure 2A). Importantly, the 2D field distribution extracted from the middle position of the PR film presents a non-uniform pattern, leading to a large LER (Figure 2F).

The 2D Fourier spectra of the optical field distribution provide further insight into these phenomena. A series of diffraction orders distributed along the k_x direction are generated by the grating mask (Figure 2G), where the spatial frequency spectrum is transformed from the magnetic field $|H_y|$ component at the collection planes (see the equations in Supplementary S4). After transmission through a smooth Ag film, only the zeroth and a pair of first diffraction orders are left in the PR film (Figure 2H). The zeroth order is the predominant component. The interference of the ±first orders produces the pattern with uniform intensity distribution. However, if the surfaces of the Ag film are rough with the RMS of 2 nm, many chaotic diffraction orders are generated and distributed randomly in the k_x–k_y space (Figure 2I). Because the superlens can transmit these unwanted diffracted orders, the pattern in the PR film is formed with poor profiles due to the complex interference of these numerous diffraction orders.

In contrast, for the HMM lithography system, the OTF of the Al/SiO_2 multilayer features a distinctive transmission window as shown in Figure 3A, which serves as a filter that only allows waves with wavevector in the range $1.5k_0 < k_x < 2.5k_0$ to pass through it. It is noted that only few resonant peaks appear in the OTF curve for the nine-layer Al/SiO_2 HMM due to the light absorption in the Al films [38–40] (further discussion is shown in Supplementary S5). According to the grating coupling equation, $k_x = nk_0\sin\theta + m(2\pi/P)$, where n is the index of substrate, k_0 is the wavevector in free space, θ is the angle of incidence, m is the order of diffraction wave and P is the period of grating. When the 365-nm light normally incidents onto

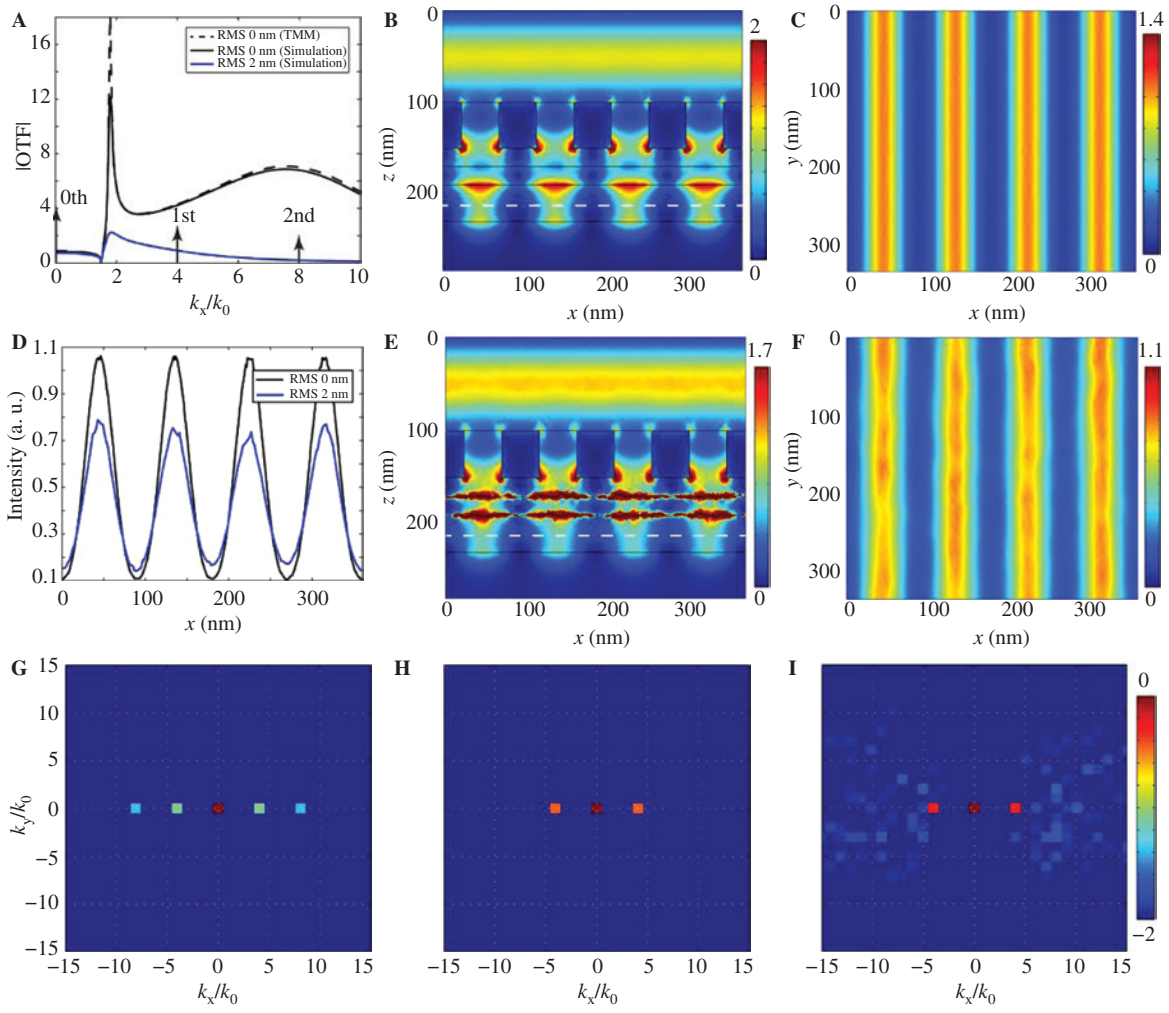

Figure 2: Effects of the rough film in superlens lithography system.
(A) OTF curves of a single Ag film with smooth and rough surfaces calculated by TMM and numerical simulation. The arrows show the positions of diffraction orders of the grating mask in *k*-space. (B) Side view and (C) top view of the normalized electric field intensity distributions with smooth Ag film (RMS = 0 nm); (E, F) corresponding simulation results with rough Ag film (RMS = 2 nm); (D) normalized electric field intensity distribution of the patterns in the PR film at the dashed line positions in (B) and (E). (G) A series of diffraction orders in *k*-space generated from the grating with a period of 90 nm. The distributions of diffraction orders in PR film after transmitted through a single Ag film with the roughness of (H) 0 nm and (I) 2 nm, respectively. The logarithm scale is used in (G)–(I).

the grating mask, only ±second-order diffraction waves with wavevectors of about $\pm 2k_0$ can pass through the multilayer, while other diffraction orders are strongly suppressed according to the OTF. Additionally, the OTF of the structure with PR and reflective Al layers involved shows a narrower passband (see Supplementary S3). Therefore, SP waves with high spatial frequency purity interfere with each other and produce a uniform PR pattern. The period of the interference pattern can be calculated by $p = P/(2m)$, which is shown in Figure 3B and C. Even after introducing roughness with RMS = 2 nm to each surface of the multilayer, the transmission performance remains spectacularly high as compared with the RMS = 0 nm case. The 2D field distribution in the middle of the PR film shows the interference pattern without obvious distortions (Figure 3E and F). Equally impressive is that the maximum intensity remains at about the same level. This behavior is in accord with the characteristics of the OTF (Figure 3A), which maintains about the same value for the rough multilayer, except that it slightly broadens at the high-*k* side (see more OTF simulations with different RMS roughness in Supplementary S6).

As a comparison, the 2D Fourier spectra can be seen in Figure 3G–I. Because of the larger period of the grating on the mask, there are more diffraction orders distributed along k_x than that in the superlens case. After transmitting through the multilayer with the RMS roughness of 0 or 2 nm, only ±second diffraction orders with equal amplitude remain. They interfere and produce uniform

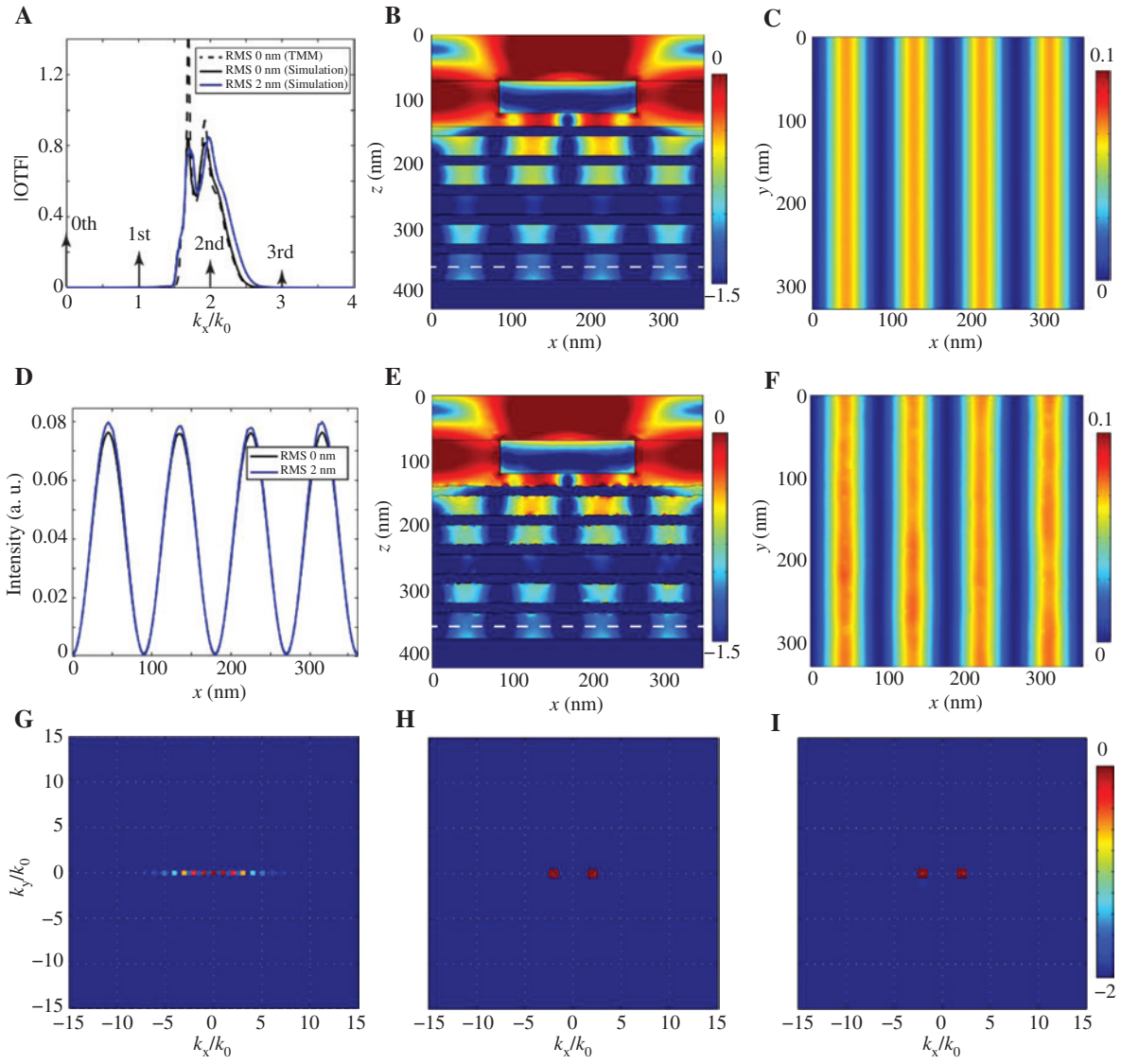

Figure 3: Effects of the rough films in HMM lithography system.
(A) OTF curves of alternating nine films of Al (15 nm)/SiO_2 (30 nm) with smooth and rough surfaces calculated by TMM and numerical simulation. The arrows show the positions of diffraction orders of the grating mask in *k*-space. (B) Side view and (C) top view of the normalized electric field intensity distributions with a smooth multilayer (RMS = 0 nm); (E, F) corresponding simulation results with a rough multilayer (RMS = 2 nm); (D) normalized electric field intensity distribution of the patterns in the PR film at the dashed line positions in (B) and (E). (G) A series of diffraction orders in *k*-space generated from grating with a period of 360 nm. The distributions of diffraction orders in the PR film after transmitted through the multilayer with the roughness of (H) 0 nm and (I) 2 nm, respectively. The logarithm scale is used in (B), (E) and (G)–(I).

patterns in the PR film with minimal effects caused by the rough films.

The LER, field intensity and field components for both systems with different surface roughness are compared in Figure 4A and B. The intensity is defined as the average peak intensity and the LER is calculated as the average RMS deviation at the positions along the sidewall of the patterns (definitions and calculations are given in Supplementary S7). For the superlens system, as the RMS roughness of the Ag film increases from 0 to 3.5 nm with 0.5 nm increments, the LER of the pattern in the PR film increases from about 0 to 1.4 nm, which is denoted by the black squares. Meanwhile, the peak intensity decreases drastically from ~1.1 to ~0.67 V^2/m^2 (denoted by the blue dots). For the HMM system, the corresponding LER increases from about 0 to 1.0 nm, which is lower than that in the superlens system. Because the loss of Al is higher than that of Ag at 365 nm wavelength, the intensity of the pattern transmitted through the HMM diminishes by more than one order of magnitude compared to that through a single Ag film. However, the intensity is stable as the surface roughness increases, which is different from the decreasing trend in the superlens system.

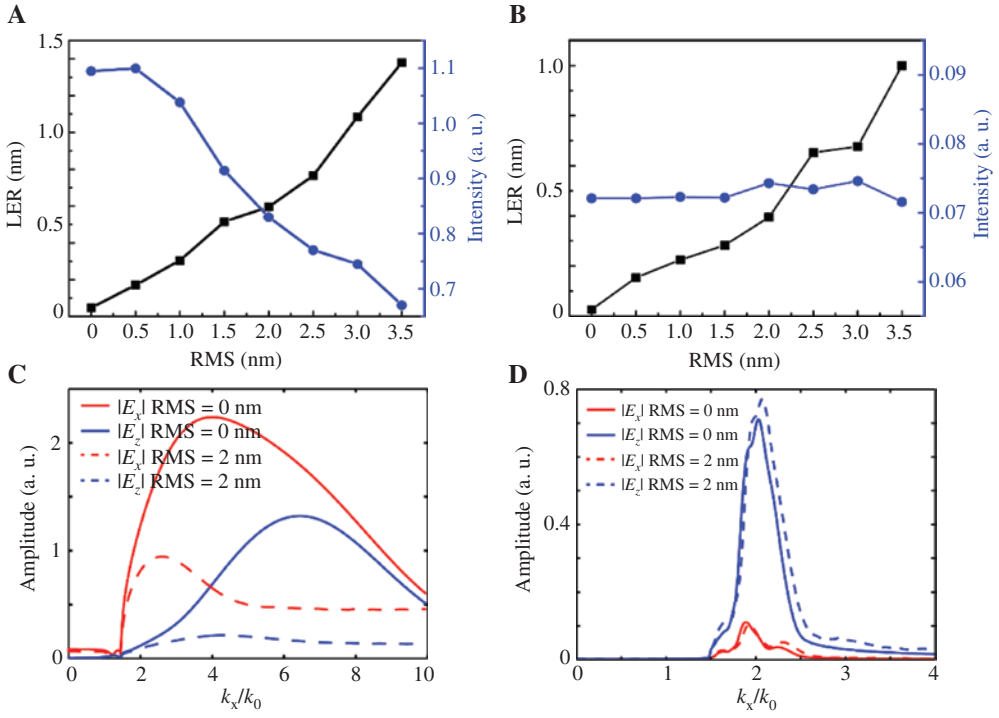

Figure 4: Comparisons of the patterning performance in both superlens and HMM systems with varied surface roughness. LER and electric field intensity variation of the patterns in the PR film as the RMS roughness increases in (A) superlens and (B) HMM, respectively. Normalized transmission amplitude of electric field components at the middle position of the PR film corresponding to the (C) superlens and (D) HMM with smooth and rough surfaces. All these data are extracted from the COMSOL simulation with the reflective layers involved in the two systems.

To further understand the impacts of the roughness in real lithography systems, the electric field is also analyzed in the simulations with the reflective layers involved. Figure 4C and D shows the electric components of the field as a function of the normalized wavevector in the two systems with and without roughness, respectively. The distributions of E_x and E_z in the superlens system and HMM system verify their corresponding broadband evanescent transmission and filtering performance. Meanwhile, the total electric field intensity of the pattern can be calculated by $|\bar{E}_x + \bar{E}_z|^2$ for a TM polarized wave, where $\bar{E}_x$ and $\bar{E}_z$ are the transmission amplitudes of the electric field components extracted from the PR film. In the high-k limit, the phase difference between the $|E_x|$ and $|E_z|$ components is about $\pi/2$, which will cause a half-pitch shift in the distribution of $|\bar{E}_x|^2$ and $|\bar{E}_z|^2$ [41, 42]. Additionally, the ratio between the electric field components $|E_x|$ and $|E_z|$ plays a crucial role in obtaining an image with high fidelity. A detailed discussion is provided in Supplementary S8. But the main conclusion is that the high $|E_x|^2/|E_z|^2$ ratio is desired to form an image with good fidelity. Considering the entire film system including the reflective layer, for the superlens structure, both $|E_x|$ and $|E_z|$ components drop drastically when the Ag layer changes from a smooth film to a rough one with the RMS roughness of 2 nm (Figure 4C), and the $|E_x|/|E_z|$ ratio for the first order clearly decreases. However, for the HMM structure, both $|E_x|$ and $|E_z|$ components hold well as the roughness increases (Figure 4D), showing its stable performance in the patterning process.

To summarize, the single Ag film has an OTF with a broad passband which allows waves in a wide range of wavevectors to transmit to the PR film. While it ensures that high-k evanescent waves reach the PR film by the coupling of SP, it also transmits the higher order waves coming from the imperfections in the thin film and the mask, which can be treated as secondary excitations of the SP waves generated by the rough surface in multiple directions (derivations are shown in Supplementary S9). The disordered diffraction waves reach the PR film and contribute to the poor profile of the PR pattern. For the HMM structure, by properly choosing the period of the mask, the desired transmission order coincides with the peak of the narrow OTF. Therefore, the light of desired spatial frequency transmits maximally, while the other diffraction orders induced by the mask and rough multilayer are relatively suppressed, leading to a more uniform pattern. Though new diffraction waves are generated in the rough multilayer, they damp dramatically because of the high

loss of the Al films and filtering effects of the HMM. This can also be seen clearly from the performances of the gratings with different periods shown in Supplementary S10. Without optimizing the mask, one may not get the benefit of spatial frequency selection. On the other hand, the superlens case does not offer such a utility because of the broad transmission of its OTF.

3 Impact of isolated defects on masks in photolithography

The quality of the mask also plays an important role in sub-diffraction lithography. The impact of defects on the mask layer is also considered in both superlens and HMM systems, where the structures are the same as before, but the grating masks have an isolated asperity (10 nm radius) as shown in Figure 5. In the superlens lithography system, the $|E_x|$ component dominates at the image side (Figure 4C and Figure S6A), meaning that the waves propagate vertically, presenting its imaging property (comparison between the two systems can be seen in Supplementary S8 and S11). Thus, the geometric feature of the isolated defect in the mask is well reproduced PR film because of its broad band superlens function, leading to a weak intensity spot in the PR pattern (Figure 5B and C). However, in the HMM lithography system, the $|E_z|$ component is dominant (Figure 4D and Figure S6C), and the ±second-order diffracted waves propagate laterally [43]. The defect mainly causes a change of phase in the interference area, and does not generate severe intensity variation in the PR film when the two SPs interfere with each other (Figure 5D and E). Therefore, the impact of a single defect on the mask layer in superlens systems is much greater than that in HMM systems. In other words, there is a tradeoff between the superlens and HMM systems. Though the superlens system offers the capability of replicating arbitrary patterns, unavoidably it is also affected sensitively by the imperfections of the thin film and the mask. On the other hand, the HMM system is more immune to such imperfections than the superlens system, but with the limitation of producing periodic patterns. Nonetheless, subwavelength dense periodic patterns have been used to evaluate lithography performance, and have many applications.

In addition, the mask with rough surfaces is also investigated in both lithography systems, which is shown in Supplementary S12. As expected, the quality of the pattern produced by the superlens system is more severely affected than that by the HMM system. Meanwhile, comparing the results of rough surfaces in both film and mask conditions, it is observed that the pattern in the PR film is more sensitive to rough films than to rough gratings.

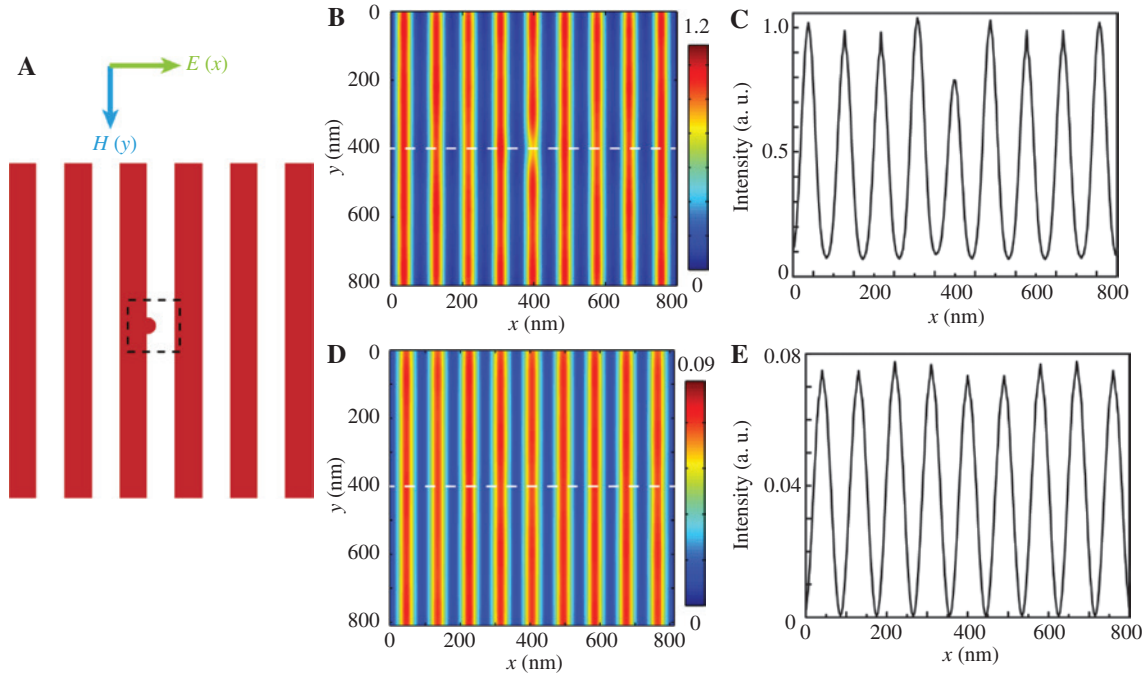

Figure 5: Impacts of isolated defects in both superlens and HMM systems.
(A) Schematic of the defective grating mask. (B, D) Normalized electric field intensity distributions extracted from the middle position of the PR film in superlens and HMM lithography systems, respectively. (C, E) Corresponding intensity distributions at the dashed line positions in (B) and (D).

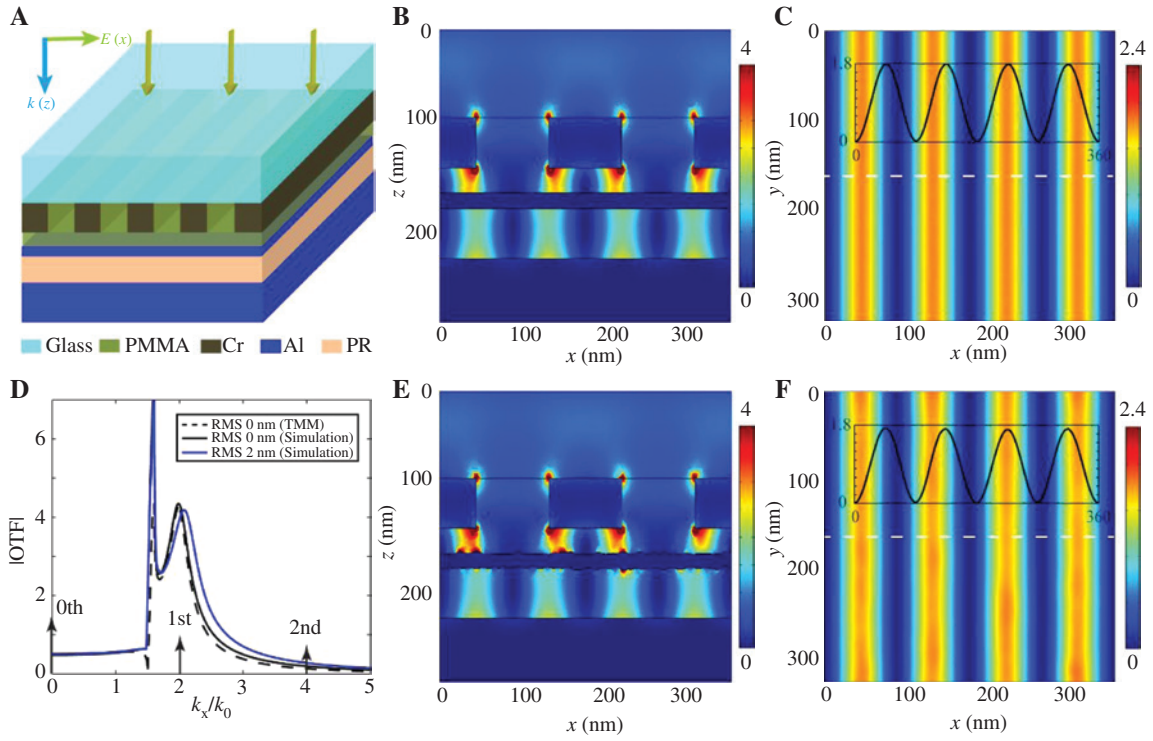

Figure 6: Effects of the rough film in waveguide lithography system.
(A) Schematics of plasmonic lithography with the waveguide structure. (B) Side view and (C) top view of the normalized electric field intensity distributions with smooth Al film (RMS = 0 nm); (D) OTF curves of a single Al film with smooth and rough surface calculated by TMM and numerical simulation. Arrows show the positions of diffraction orders of the grating mask in *k*-space. (E, F) Corresponding simulation results with rough Al film (RMS = 2 nm). The inset pictures in (C) and (F) are the corresponding intensity distributions at the dashed line positions.

4 Interference lithography by integrating PR as an optical waveguide

To validate the generality of the above conclusion, we carried out a similar analysis in a recently reported plasmonic lithography scheme that demonstrated large area uniform periodic patterns with linewidth 1/6 of the wavelength and an aspect ratio of 2:1 [30]. Though the structure is almost identical to the superlens system, the thin metal film serves a totally different function: it is used to filter out the unwanted diffraction orders. The PR layer is much thicker, which functions as the core of an optical waveguide. The propagation constant of the waveguide mode matches that of the ±first-order diffracted waves generated by the periodic mask. Therefore, the system has an inherent spatial frequency selection property, which explains the observed uniform and high aspect ratio pattern over a cm^2 area. Figure 6 shows a waveguide lithography system with the transmission medium composed of a single Al film (12 nm thick). In our analysis, we take the period of the grating mask to be 180 nm, and only the ±first order of the diffracted waves can pass through, but the zeroth and other high orders are blocked. As expected, the pattern in the PR film with a period of 90 nm shows high contrast and straight edges, and this performance is less affected by the rough surfaces of the Al film with the RMS of 2 nm. This behavior further confirms the foregoing analyses.

5 Conclusions

Two plasmonic lithography systems with rough films are simulated and analyzed systematically. For the superlens system, as the surface roughness of the Ag film increases, the LER of the patterned PR grows gradually, and the corresponding intensity decreases dramatically. This behavior is ascribed to the broad passband of the Ag film and the localized SP scattered by the rough surface, which result in poor profiles on the patterns. In contrast, the OTF of the HMM system presents a function of spatial frequency selection, which suppresses the impacts of rough surfaces and leads to steady interference with the selected diffracted waves. As a result, with the surface roughness on the Al/SiO_2 multilayer, the LER of the pattern imaged by the HMM increases

slightly while the field intensity is stable. Additionally, the HMM system is more tolerant to the defects on the mask. The benefits of this filtering-based design are also verified by a waveguide lithography system. Therefore, spatial frequency selection is an optimal way to construct periodic patterns in subwavelength lithography. In addition, the same metal can function differently in different schemes and wavelength ranges. For example, the thin Al film functions as a spatial frequency filter in the foregoing analyses, but works as a superlens in the deep ultraviolet range [44]. In Supplementary S13, an Al film-based superlens system is capable of imaging at the wavelength of 193 nm, which also presents sensitivity to the roughness due to its broad passband of evanescent waves. These analyses give new insights into plasmonic nanopatterning, and can be a useful guideline in designing future plasmonic lithography systems.

6 Supplementary material

The supplementary material is available online on the journal's website or from the author.

Acknowledgments: The authors thank Long Chen for helpful discussions. This work was supported by the National Science Foundation (grant no. CMMI-1537440).

References

[1] Barnes WL, Dereux A, Ebbesen TW. Surface plasmons subwavelength optics. Nature 2003;424:824–30.
[2] Wu YKR, Hollowell AE, Zhang C, Guo LJ. Angle-insensitive structural colors based on metallic nanocavities and coloured pixels beyond the diffraction limit. Sci Rep 2013;3:1194.
[3] Ye F, Merlo JM, Burns MJ, Naughton MJ. Optical and electrical mappings of surface plasmon cavity modes. Nanophotonics 2014;3:33–49.
[4] Pendry JB. Negative refraction makes a perfect lens. Phys Rev Lett 2000;85:3966–9.
[5] Fu YQ, Zhou XL. Plasmonic lenses: a review. Plasmonics 2010;5:287–310.
[6] Fang N, Lee H, Sun C, Zhang X. Sub-diffraction-limited optical imaging with a silver superlens. Science 2005;308:534–7.
[7] Berger SD, Gibson JM, Camarda RM, et al. Projection electron-beam lithography: a new approach. J Vac Sci Technol B 1991;9:2996–9.
[8] Drachev VP, Chettiar UK, Kildishev AV, et al. The Ag dielectric function in plasmonic metamaterials. Opt Express 2008;16:1186–95.
[9] Kildishev AV, Borneman JD, Chen KP, Drachev VP. Numerical modeling of plasmonic nanoantennas with realistic 3D roughness and distortion. Sensors 2011;11:7178–87.
[10] Trügler A, Tinguely JC, Krenn JR, Hohenau A, Hohenester U. Influence of surface roughness on the optical properties of plasmonic nanoparticles. Phys Rev B 2011;83:081412(R).
[11] Gómez-Gómeza M, Calderóna J, Abarguesb R, et al. An advance towards the synthesis of Ag nanorod arrays with controlled surface roughness for SERS substrates. Mater Today: Proc 2016;3:294–302.
[12] Huang SW, Wang HG, Ding KH, Tsang L. Subwavelength imaging enhancement through a three-dimensional plasmon superlens with rough surface. Opt Lett 2012;37:1295–7.
[13] Wang HG, Bagley JQ, Tsang L, et al. Image enhancement for flat and rough film plasmon superlenses by adding loss. J Opt Soc Am B 2011;28:2499–509.
[14] Guo Z, Huang Q, Wang C, et al. Negative and positive impact of roughness and loss on subwavelength imaging for superlens structures. Plasmonics 2014;9:103–10.
[15] Rho J, Ye ZL, Xiong Y, et al. Spherical hyperlens for two-dimensional sub-diffractional imaging at visible frequencies. Nat Commun 2010;1:143.
[16] Liang GF, Zhao ZY, Yao N, et al. Plane demagnifying nanolithography by hybridhyperlens-superlens structure. J Nanophotonics 2014;8:083080.
[17] Xu T, Agrawal A, Abashin M, Chau KJ, Lezec HJ. All-angle negative refraction and active flat lensing of ultraviolet light. Nature 2013;497:470–4.
[18] Liang GF, Wang CT, Zhao ZY, et al. Squeezing bulk plasmon polaritons through hyperbolic metamaterials for large area deep subwavelength interference lithography. Adv Opt Mater 2015;3:1248–56.
[19] Shivanand S, Ludwig A, Webb KJ. Impact of surface roughness on the effective dielectric constants and subwavelength image resolution of metal-insulator stack lenses. Opt Lett 2012;37:4317–9.
[20] Schøler M, Blaikie RJ. Simulations of surface roughness effects in planar superlenses. J Opt A: Pure Appl Opt 2009;11:105503.
[21] Zhang C, Zhao D, Gu D, et al. An ultrathin, smooth, and low-loss Al-doped Ag film and its application as a transparent electrode in organic photovoltaics. Adv Mater 2014;26:5696–701.
[22] Gu D, Zhang C, Wu YK, Guo LJ. Ultra-smooth and thermally-stable Ag-based thin films with sub-nanometer roughness by Al doping. ACS Nano 2014;8:10343–51.
[23] Zhao DW, Zhang C, Kim H, Guo LJ. High-performance Ta2O5/Al-doped Ag electrode for resonant light harvesting in efficient organic solar cells. Adv Energy Mater 2015;5:1500768.
[24] Gao P, Yao N, Wang CT, et al. Enhancing aspect profile of half-pitch 32 nm and 22 nm lithography with plasmonic cavity lens. Appl Phys Lett 2015;106:093110.
[25] Choi WK, Liew TH, Dawood MK, et al. Synthesis of silicon nanowires and nanofin arrays using interference lithography and catalytic etching. Nano Letters 2008;8:3799–802.
[26] Campbell M, Sharp DN, Harrison MT, Denning RG, Turberfield AJ. Fabrication of photonic crystals for the visible spectrum by holographic lithography. Nature 2000;404:53–6.
[27] Yang Y, Li Q, Wang GP. Design and fabrication of diverse metamaterial structures by holographic lithography. Opt Express 2008;16:11275–80.
[28] Zhang XP, Ma XM, Dou F, Zhao PX, Liu HM. A biosensor based on metallic photonic crystals for the detection of specific bioreactions. Adv Funct Mater 2011;21:4219–27.

[29] Smelser CW, Grobnic D, Mihailov SJ. Generation of pure two-beam interference grating structures in an optical fiber with a femtosecond infrared source and a phase mask. Opt Lett 2004;29:1730.
[30] Chen X, Yang F, Zhang C, Zhou J, Guo LJ. Large-area high aspect ratio plasmonic interference lithography utilizing a single high-k mode. ACS Nano 2016;10:4039–45.
[31] Podolskiy V, Narimanov EE. Near-sighted superlens. Opt Lett 2005;30:75–7.
[32] Arnold MD, Blaikie RJ. Subwavelength optical imaging of evanescent fields using reflections from plasmonic slabs. Opt Express 2007;15:11542–52.
[33] Palik ED. Handbook of optical constants of solids. New York, Academic Press, 1991.
[34] Johnson PB, Christy RW. Optical constants of noble metals. Phys Rev B 1972;6:4370–9.
[35] Leong ES, Liu YJ, Wang B, Teng J. Effect of surface morphology on the optical properties in metal-dielectric-metal thin film systems. ACS Appl Mater Interfaces 2011;3:1148.
[36] Katsidis CC, Siapkas DI. General transfer-matrix method for optical multilayer systems with coherent, partially coherent, and incoherent interference. Appl Opt 2002;41:3978–87.
[37] Skorobogatiy M. Wave propagation in planar anisotropic multilayers, transfer matrix formulation, nanostructured and subwavelength waveguides: fundamentals and applications, Chichester, UK, John Wiley & Sons, 2012, 39–45.
[38] Cortes CL, Newman W, Molesky S, Jacob Z. Quantum nanophotonics using hyperbolic metamaterials. J Opt 2012;16:1013–20.
[39] Ferrari L, Wu C, Lepage D, Zhang X, Liu Z. Hyperbolic metamaterials and their applications. Prog Quant Electron 2015;40:1–40.
[40] Drachev VP, Podolskiy VA, Kildishev AV. Hyperbolic metamaterials: new physics behind a classical problem. Opt Express 2013;21:15048.
[41] Zhao Z, Luo Y, Zhang W, et al. Going far beyond the near-field diffraction limit via plasmonic cavity lens with high spatial frequency spectrum off-axis illumination. Sci Rep 2015;5:15320.
[42] Zhang W, Wang H, Wang CT, et al. Elongating the air working distance of near-field plasmonic lens by surface plasmon illumination. Plasmonics 2015;10:51–6.
[43] Zhu P, Shi HF, Guo LJ. SPPs coupling induced interference inmetal/dielectric multilayer waveguides and its application for plasmonic lithography. Opt Express 2012;20:12521–9.
[44] Schilling A, Schilling J, Reinhardt C, Chichkov B. A superlens for the deep ultraviolet. Appl Phys Lett 2009;95:121909.

Supplemental Material: The online version of this article offers supplementary material (https://doi.org/10.1515/nanoph-2017-0028).